Journal of Materials Research and Technology 33 (2024) 6701–6713

Contents lists available at ScienceDirect

Journal of Materials Research and Technology

journal homepage: www.elsevier.com/locate/jmrt

Wetting behaviour of nickel-based brazing alloy BNi-5a on conventionally cast and laser-melted austenitic stainless steel 316L

W. Tillmann [a], J. Bültena [a,*], L. Wojarski [a], J. Zajaczkowski [a], K. Donnerbauer [b], F. Walther [b]

[a] Institute of Materials Engineering, TU Dortmund University, 44227, Dortmund, Leonhard-Euler-Straße 2, Germany
[b] Chair of Materials Test Engineering, TU Dortmund University, 44227, Dortmund, Baroper Straße 303, Germany

ARTICLE INFO

Handling editor: L Murr

Keywords:
Additive manufacturing
PBF
Brazing
Stainless steel
Nickel base brazing alloy
Wetting
Atomic force microscopy

ABSTRACT

Laser beam melting is an additive manufacturing process that enables the production of highly complex components. In this process, metal powder is locally melted using a laser beam and built up layer by layer to form a physical component. Due to the layer-by-layer process manufacturing technique of the additive manufacturing process, the microstructure of a laser-melted 316L austenitic stainless steel differs from that of a conventionally cast material. For brazing technology, the different microstructure morphology is important because it affects the known wetting and diffusion behavior with a brazing filler metal, which affects the ability to produce high-strength brazed joints. Brazeability can be determined by examining the wetting of the brazing filler metal with the material to be joined. Therefore, this study investigates the wetting behavior of nickel-base brazing alloy BNi-5a on conventionally cast and laser-melted 316L austenitic stainless steel. Wetting tests were performed to evaluate the spreading area and wetting angle of BNi-5a on both 316L substrates. The wetting tests were performed in a high-temperature vacuum furnace at 1190 °C for 15 min. The results show that the laser-melted 316L stainless steel exhibits enhanced wettability compared to the conventionally cast material. This is related to a higher surface energy and a more pronounced diffusion mechanism called grain boundary grooving on the surface of the material.

1. Introduction

Additive manufacturing encompasses a range of manufacturing processes in which components are produced directly from digital 3D models and shapeless raw materials [1,2]. One such process is laser beam melting *(powder bed fusion of metals with laser beam, PBF-LB/M)*. In this process, metal powder is melted locally using a laser beam and built up layer by layer to form a physical component [3]. This enables the production of highly complex components with great precision and a high degree of design freedom [2]. Stainless steels, such as the austenitic chromium-nickel steel 316L, are the most commonly produced steel grade with this process [3].

The high costs, long production times, limited variety of materials and size limitations represent obstacles to the widespread industrial use of laser-melted components [2,4–7]. Hybrid components offer a potential solution to these challenges. They consist of parts made through both conventional methods (e.g., casting and subtractive processes) and laser beam melting. The parts can be joined together into a hybrid component by means of brazing in a vacuum furnace [8,9].

Brazing is a manufacturing process in which solid base materials are joined together using a molten material, the brazing filler metal [10]. One of the advantages of using brazing for the production of hybrid components is the capacity to combine a virtually limitless range of materials. This eliminates the constraints imposed by the limited material variety of the laser-melting process. Furthermore, the utilization of brazing technology has the potential to improve the efficiency of the entire production chain for hybrid components. This potential is a consequence of the production route of laser-melted parts. These are typically subjected to heat treatment subsequent to the additive manufacturing process to reduce thermal residual stresses [3]. In the case of laser-melted stainless steel 316L this heat treatment usually includes a solution annealing process. This process is generally conducted at temperatures above 1000 °C [11–13] and can be integrated into a brazing cycle if a suitable brazing filler metal is used.

Nickel-based brazing filler metals are frequently applied in the brazing of stainless steels [14,15]. The term "nickel-based brazing filler metals" refers to a diverse range of alloy systems, in which the elements silicon, boron, chromium and/or phosphorus are added to reduce the

* Corresponding author.
E-mail address: julia.bueltena@tu-dortmund.de (J. Bültena).

https://doi.org/10.1016/j.jmrt.2024.10.228
Received 9 September 2024; Received in revised form 25 October 2024; Accepted 28 October 2024
Available online 30 October 2024

melting point of the main alloying element nickel [14]. This enables a brazing temperature below the melting temperature of stainless steels.

The brazing temperature of nickel-based brazing filler metals are already within the range of the solution heat treatment temperature of austenitic stainless steel 316L [16]. Consequently, the solution annealing process of laser-melted 316L parts can be carried out directly at brazing temperature, thereby reducing the overall production time of hybrid components.

The microstructure of a laser-melted 316L differs from that of a conventionally cast material [9]. The conventionally cast material is distinguished by an isotropic material structure, exhibiting discernible twin grain boundaries. In contrast, the microstructure of the laser-melted 316L is anisotropic. As a consequence of the layer-by-layer nature of the additive manufacturing process, the locally melted paths of the laser beam are discernible in the material structure. In addition, micro-grains grow across the boundaries of each melt path. Inside these micro-grains, a hexagonal, cellular substructure is evident. Notably, the grain size of this cellular substructure is significantly smaller than that of the conventionally cast material [9,17,18].

Solution annealing causes the morphology of the laser-melted 316L to approximate that of a conventionally cast material. This refers to the dissolution of both the individual melt paths and the cellular substructure [9].

For the production of a high strength brazed joint wetting between the brazing filler metal and the base material to be joined is essential [10,19]. The quality of the wetting is related to the microstructure of the material [10,19]. Due to the differences in microstructures between the conventionally cast and laser-melted 316L alloy, it is expected that the wetting will differ depending on the manufacturing route. A solution annealing process may be employed not only to align the additive microstructure morphology with that of the conventional material but also to approximate the wetting behavior of the brazing filler metal to that of conventionally cast materials.

In brazing, wetting tests are used to evaluate the wetting behavior of a brazing filler metal with a base material [20]. In these tests, a defined amount of the brazing filler metal is applied to the base material and melted within a brazing cycle [20]. The criteria for evaluating wetting are the spreading area [21,22] and the wetting angle between the brazing alloy and the base material [20]. Good wetting is achieved when the spreading area of the brazing alloy is large and the wetting angle between the brazing alloy and the base material is less than 90° [20]. If both of these criteria are met, it is possible to obtain a load bearing brazed joint [20]. A detailed description of the wetting test method and criteria for evaluation can be found in Refs. [10,19,20].

The wetting of nickel-based brazing filler metals on continuously cast stainless steels has been extensively studied. These studies typically describe the wetting as good to very good [15,22–25]. In vacuum furnace brazing, the wetting angle between a nickel-based brazing alloy and a conventionally cast stainless steel is usually below 15° [23,26]. In contrast, the wetting behavior of the lase-melted 316L is unknown.

In general, there are very few studies available in the literature that deal with the wetting of laser-melted materials. Only Liu and Hao carried out in-situ wetting tests on a heating stage under an argon atmosphere with the laser-melted titanium alloy Ti6Al4V [27,28]. The research group used the nickel-based brazing filler metal B–Ni2 [27] and the active brazing filler metal AgCuTi for their investigations [28]. Within the scope of the investigations, the authors analyzed the influence of the brazing temperature and the brazing time on the wettability of the laser-melted Ti6Al4V. The wetting of the laser-melted Ti6Al4V by the brazing filler metals B–Ni2 and AgCuTi was sufficient to produce a load-bearing brazed joint. As there was no detailed comparison of the wetting of a conventionally cast and a laser-melted Ti6Al4V alloy, no difference in the wetting behavior depending on the manufacturing route were identified.

Despite the known factors influencing wetting, there are few studies comparing the wetting behavior of conventional and laser-melted materials. For this reason, the wettability of the laser-melted stainless steel 316L by brazing alloy B–Ni5a is investigated and compared with that of the conventionally cast material. The 316L stainless steel was chosen because it has been well researched in both, additive manufacturing and brazing technology [2,19].

2. Methods

2.1. Base materials

For the experiments, 316L austenitic stainless steel was purchased from the conventional production route using continuous casting and the laser beam-melting route. The conventional manufactured material was a cold-rolled, solution-annealed 316L round bar (Ø 20 mm) according to DIN EN 10088-3. The raw material for the laser melting process was spherical 316L powder with a particle size distribution of $-45 + 10$ µm. Table 1 shows the chemical composition of the metal powder and the conventional rod material.

The metal powder was processed into semi-finished parts with a layer thickness of 30 µm (Ø 20 mm, height 87 mm). The SLM 280 H L production system from SLM Solutions was used. Optimized data sets from the system manufacturer were utilized as process parameters.

2.2. Brazing filler metal

To evaluate the wettability of the base materials the nickel-based brazing filler metal B–Ni5a was used (standardized to AWS A5.8). The brazing filler metal was a foil with a thickness of 25 µm. The chemical composition is given in Table 2. The brazing temperature recommended by the manufacturer is in the range 1170–1200 °C [29].

2.3. Wetting tests

Wetting tests were performed to determine the wettability of the conventional and the laser-melted base materials. In these tests, a defined amount of brazing filler metal was applied onto the base materials surface and melted in a brazing cycle. During the brazing cycle, the filler metal spreads out on the material surface and solidifies.

2.3.1. Sample geometry and number of samples

For the wetting tests, the conventional rod material and the laser-melted semi-finished parts were cut into 5 mm thick discs by wire erosion. The surface of the discs was ground to N6 quality (ISO 1302) to standardize the initial condition. Three conventional and six laser-melted discs were produced for wetting tests.

Laser-melted materials are often heat treated after the manufacturing process to reduce residual thermal stresses [3]. To account for this post-treatment, three of the six laser-melted discs were solution annealed at 1020 °C for 60 min in a high vacuum ($<10^{-4}$ mbar). The brazing furnace used for this purpose was the Schmetz EU 80/1H. The annealing temperature and duration were in accordance with other research [12,13,30].

The remaining three laser-melted discs were left in their as-built state. This material condition is interesting for brazing technology because the brazing temperature of the B–Ni5a filler metal is in the solution annealing range of the 316L alloy. If the wettability of this base material condition is sufficient, brazing and solution annealing can be combined in a single process step.

The microstructural analysis of the conventional cast and laser-melted base materials in the as-built and solution annealed condition were part of previous work and can be found in Ref. [9].

2.3.2. Wetting test process

Prior to the wetting tests, all samples were cleaned in an ultrasonic ethanol bath for 5 min. The B–Ni5a brazing foil was punched to a diameter of 3 mm and was also cleaned with ethanol. Two layers of the

Table 1
Chemical Composition of the Base Materials according to certificates [wt-%].

Material	C	Si	Mn	P	S	N	Cr	Ni	Mo	O
Conventional	0.021	0.5	1.72	0.044	0.022	0.069	16.65	10.11	2.06	–
PBF-LB/M-Powder	0.02	0.69	0.82	0.01	0.01	0.09	17.75	12.6	2.38	0.02

Table 2
Chemical composition of the brazing filler metal B–Ni5a [wt-%].

Material	Ni	Cr	Si	B
B–Ni5a (Ni 660)	72.5	19.0	7.25	1.25

brazing foil were then placed in the center of a wetting sample. The amount of brazing filler metal applied was 0.0028 g.

The wetting tests were performed under high vacuum ($<10^{-4}$ mbar) in the EU 80/1H furnace from Schmetz. The heating rate was 10 °C per minute. During heating, there were two 15-min holding phases at 450 °C and 1015 °C. These holding phases were used to ensure a homogeneous temperature distribution of the furnace batch. Brazing was done at 1190 °C for 15 min. The brazing temperature is in the upper range of the solution annealing temperature of the 316L alloy. Cooling was achieved with nitrogen gas cooling at 4 bar overpressure to prevent chromium carbide precipitation.

2.3.3. Evaluation of the wetting tests

The evaluation of the wetting tests included light microscopic imaging, a measurement of the spreading area of the solidified brazing alloy, a determination of the contact angle between the solidified brazing alloy and the base material and a microstructure analysis.

2.3.4. Light microscopic images and spreading area of brazing alloy

Light microscope images of each wetting sample were taken using a Leica DVM6 digital microscope (objective: PlanAPO FOV 43.75; 0.215× magnification; image resolution: 18 μm per pixel). The spreading area was determined using the software "MountainsMap8" from DigitalSurf.

2.3.5. Contact angle between brazing alloy and base material

To determine the contact angle, a 3D image of the solidified brazing alloy on the wetting samples was taken using the Infinite Focus G5 digital microscope from Alicona (5× magnification, vertical resolution: 0.306 μm per pixel, lateral resolution: 7.828 μm per pixel). With the help of the software "MountainsMap8" from DigitalSurf, three profiles of the solidified braze droplet were extracted from the 3D image, each offset by 120°. The contact angle between the brazing alloy and the base material was measured at the ends of these profiles. Six contact angles per wetting sample were measured and arithmetically averaged.

2.3.6. Microstructural analysis

During the wetting tests, reaction and diffusion processes occur between the filler metal and the base material. These processes influence the solidification behavior of the brazing filler metal and lead to the formation of new phases.

In order to analyze the phase formation, the wetting samples were examined under a scanning electron microscope (SEM) in the top view and in the cross section. The cross sections were taken along the center of the solidified braze alloy. The SEM examinations were performed with a JXA-iHP200F microprobe from JEOL at 100× magnification in the top view and 1000× magnification in the cross section. The chemical composition of the phases was analyzed by wavelength dispersive X-ray spectroscopy (WDX) in the cross section.

2.4. Surface energy

The wetting tests revealed significant differences in wettability between the laser-melted and the conventionally cast 316L. According to Young's theory, wettability is related to surface energy [31]. Therefore, the surface energy of the different base materials was determined by contact angle measurement according to DIN EN ISO 19403-2 [32]. The contact angle measuring instrument OCA 15 from DataPhysics Instruments GmbH was used for this purpose. In a contact angle measurement, the contact angle between the surface of a material and one or more test liquids is measured. The surface energy is then calculated from the measured contact angles and the surface tension of the test liquid(s) [32,33].

In this study, the surface energy was analyzed on three samples per base material (conventional, PBF-LB/M in the as-built and solution-annealed condition). The base materials were in their original state prior to brazing. Water and dichloromethane were used as test liquids. The analyses were carried out using the OWRK method [32] with the software integrated in the contact angle measuring instrument. Each sample was measured three times and the results were arithmetically averaged.

2.5. Atomic force microscopy (AFM)

The microstructural analysis of the wetting samples indicated the formation of grain boundary grooves on the surface of the base materials after the brazing process. These grain boundary grooves could induce capillary action and thus affect the wettability of the base materials [20]. To verify the presence of grain boundary grooves, atomic force microscopy (AFM) measurements were performed on conventionally cast and laser-melted material surfaces. Therefore, samples with a wetting sample geometry were used. These samples were ground to a surface quality of N1 (Ra = 0.025 μm, according to ISO 1302). This high surface quality allowed the topography to be measured without being affected by roughness peaks. As it has been assumed that the grain boundary grooves formed during the brazing process, the samples were exposed to the brazing cycle of the wetting tests. Subsequently, the topography of 10 grain boundaries on the surface of each sample were measured by AFM. The measurements were carried out using Litescope™ AFM from Nenovision. This AFM was installed in a scanning electron microscope (SEM, Crossbeam XB 550L from Zeiss) [34,35]. The AFM was equipped with an Akiyama measuring probe (Typ A-PROBE-10) from NanoWorld AG. The probe has a measuring tip with a radius of less than 15 nm. The topography of a potential grain boundary groove was measured in the tapping mode of the AFM using setpoints of approx. 5 Hz. The measuring needle moved line by line over the grain boundary, scanning the measuring area in a planar manner. The measurement parameters are listed in Table 3.

The result of a topographic measurement was a three-dimensional planar surface profile (length: 10 μm, width: 1 μm). A linear profile was extracted from each planar surface profile using the MountainsMap8 software from DigitalSurf, see Fig. 1. For each linear profile the parameters width, depth and opening angle were determined. In addition to the topographical image, an SEM image was taken of each measuring area at 10,000× magnification in secondary electron contrast.

The width w and depth h of a groove were measured directly on the extracted profile using the MountainsMap8" evaluation software. Direct measurement of the opening angle β was not possible. Therefore, the opening angle β was calculated for each groove using the following geometric relationships: $\beta = 180^{\infty} - 2 \cdot \tan^{-1}\frac{h}{0{,}21 \cdot w}$. The geometric re-

Table 3
Measurement parameters of atomic force microscopy (AFM).

Distance between the measuring lines: 20 nm
Traversing speed of the measuring needle: 0.5 and 1.5 μm/s
Resonant frequency of the probe: 44795 1/s

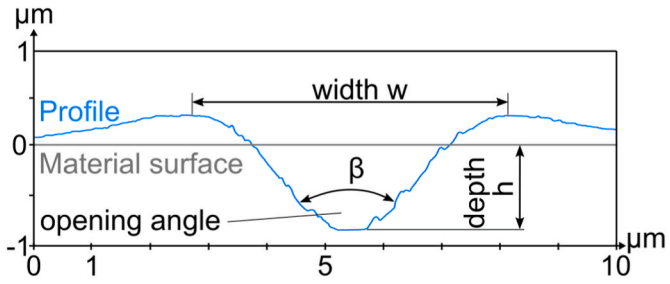

Fig. 1. Topography of a grain boundary groove.

lations and the derivation of the equation can be found in Ref. [36].

3. Results

3.1. Wetting surface

Fig. 2 shows light microscope images of the wetting samples. For illustrative reasons, the conventional wetting sample is abbreviated as C, the laser-melted sample in the as-built state as PBF and the solution-annealed condition as PBFHT.

The light microscopic images reveal a larger surface of the brazing alloy on the wetting samples of the laser-melted materials (PBF, PBFHT). The optically visible results are confirmed by the measurement of the spreading area and the contact angle, see Fig. 3.

The average spreading area of the brazing filler metal on the conventionally cast material is $9700 \cdot 10^3 \pm 1069$ mm^2/g. The average contact angle is 2.5 ± 0.3°. These values correspond to Rabinkin's literature data for vacuum furnace brazing of austenitic chromium-nickel steels [23,26].

In the as-built condition the spreading area of the brazing filler metal on the laser-melted material is $16{,}500 \cdot 10^3 \pm 1045$ mm^2/g. This is 70% larger than the spreading area of the conventional material. In contrast, the spreading area on the solution-annealed material state is $16{,}300 \cdot 10^3 \pm 760$ mm^2/g. Due to the scatter of the measurement results, no difference in the spreading behavior between both laser-melted material states is discernible. The same applies to the wetting angle, which is 1.2 ± 0.3° for both material conditions. This contact angle is 48 % lower than that of the conventionally cast material. In this regard, a larger spreading area of the brazing filler metal and the smaller contact angle indicates a better wettability of the laser-melted 316L.

Part of this study is to explain the cause for this enhanced wettability. It is noticeable, that both laser-melted material states exhibit the same wettability. As a result of the prior heat treatment, the microstructure of the laser-melted material was aligned with the conventional material [9]. However, this does not affect the wettability of the additive material. The reason for this will be explained later in this study.

3.2. Surface energy

One reason for the enhanced wettability of the laser-melted 316L may be the energy of the joining surface. In brazing, the surface energy is decisive, as it directly affects the contact angle and the spreading area of the brazing filler metal [32]. A higher surface energy leads to a smaller contact angle and a larger spreading area. This results in a better wettability. To verify that the surface energy of the laser-melted material was the cause of the enhanced wettability, it was quantified for all the base materials studied. The results are shown in Fig. 4.

The average surface energy of the conventionally cast material is 29.9 ± 4.6 mN/m. This value is within the range of values reported in the literature [37]. In contrast, the surface energy of the laser-melted material in the as-built condition is significantly higher at 38.5 ± 10.1 mN/m. Compared to the conventionally cast material, the measurement results show greater standard deviation. The reason for this is a higher and more variable defect density in the additive crystal lattice from the bottom to the top a laser-melted part. Various studies have demonstrated that the laser-melted 316L exhibits a smaller grain size, micro-segregations and a higher dislocation density in comparison to the conventionally cast material [18,38].

The application of a heat treatment process has been shown to reduce the number of defects in the crystal lattice as a result of recrystallization processes [30]. Therefore, the average surface energy of the solution-annealed laser-melted material and the standard deviation is reduced to 30.8 ± 5.9 mN/m. Furthermore, the surface energy is almost identical to that of the conventionally cast material. This reflects the alignment of the laser-melted material structure with the conventional material due to the heat treatment.

The higher surface energy in the as-built state of the additve material is presumed to be one reason for the enhanced wettability of the laser-melted 316L. However, the measurement results indicate that the surface energy is 25 % lower in the solution-annealed condition. According to Young, this should be accompanied by a lower wettability of the solution-annealed material. However, the investigations show an equivalent wettability of both laser-melted material states. Therefore, the surface energy cannot be the only factor responsible for the enhanced wettability of the laser-melted 316L. Other mechanisms, such as local interactions between the brazing filler metal and the base

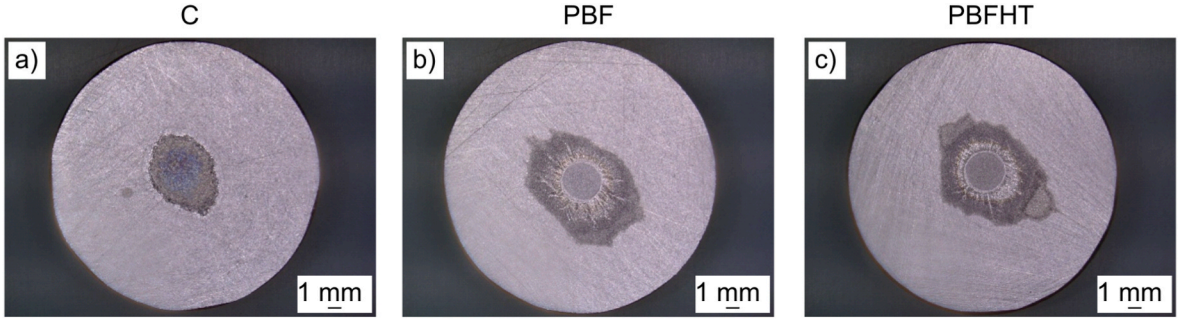

Fig. 2. Light microscope images of the wetting samples.

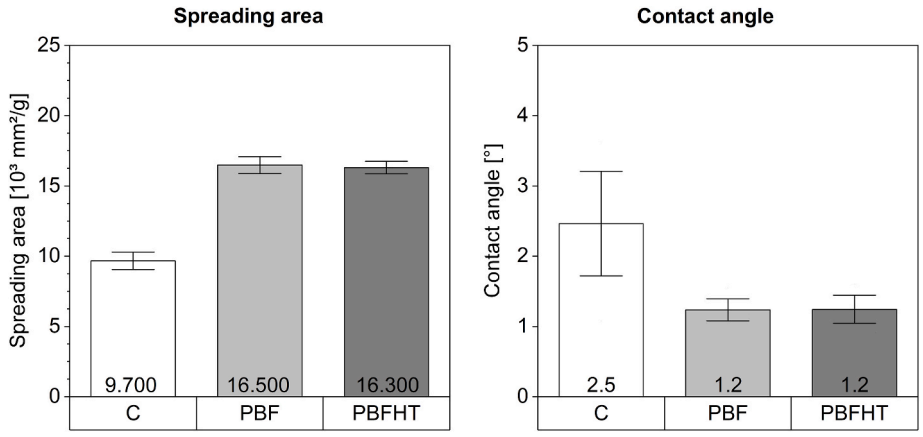

Fig. 3. Spreading area and contact angle.

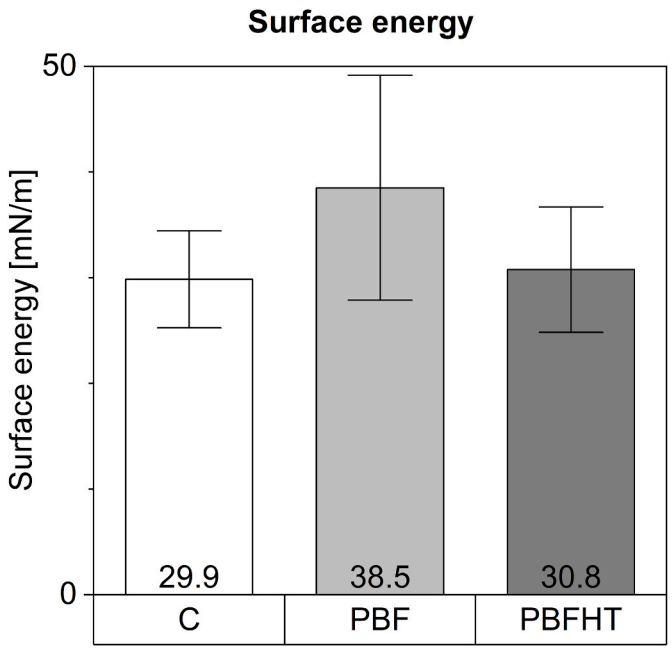

Fig. 4. Surface energy.

material or diffusion phenomena at the joining surface, could superimpose the influence of the surface energy and therefore play a decisive role in the wettability of the laser-melted 316L alloy.

3.3. Microstructure of the brazing alloy on the wetting samples

3.3.1. Conventional wetting samples

The light microscopic images of the wetting samples in Fig. 2 show a different solidification morphology of the brazing filler metal on the laser-melted 316L compared to the conventionally cast material. While the brazing filler metal on the conventional base material solidifies in a circular to oval shape, the shape of the solidified brazing filler on the additive material is irregular. The only common feature at both base materials is a circular area in the center of the solidified droplet. This area corresponds to the location of the brazing filler metal application.

The location of the brazing filler metal application is also visible under scanning electron microscopic inspection. Fig. 5 shows the microstructure of the brazing alloy on a conventional wetting sample in a top view (top) and in a cross-section (bottom).

On the conventional sample, the solidified brazing filler metal has a domed shape. It solidifies as an equiaxial dendritic nickel solid solution with the chemical composition determined by WDX shown in Table 4. The dome shape is also evident in the cross-sections in Fig. 5b to d and results in a larger brazing filler metal volume in the center of the droplet compared to the edge. Due to the lower filler metal volume, the brazing metal solidifies from the edge towards the center. This can be seen in Fig. 5a.

As the brazing filler volume increases, chromium borides are precipitated at the grain boundaries of the base material. This can be seen in Fig. 5b and c. The depth of the chromium boride precipitations increases toward the center of the solidified droplet.

Despite the presence of chromium borides in the base material, nickel silicides and chromium borides are precipitated at the top of the nickel solid solution in the area of the brazing filler metal application. The chemical composition of these phases is also shown in Table 4. The formation of nickel silicides and chromium borides has been documented several times in the literature [19,26,39]. These phases are formed due to the limited solubility of the nickel solid solution for silicon and boron. The proportion of these elements increases as the volume of the filler metal increases from the edge to the center of the solidified droplet. Since the nickel solid solution can no longer dissolve them, chromium borides and nickel silicides are precipitated.

3.3.2. Laser-melted wetting samples

Fig. 6 shows the top view of the laser-melted wetting samples in scanning electron microscopic images. The as-built condition is shown at the top, and the solution-annealed material state at the bottom.

The cross-sections corresponding to the top views are shown in Fig. 7. The images show the morphology of the brazing alloy from the center to the edge of the solidified brazing droplet.

All SEM images confirm that there are no significant differences between the laser-melted material in the as-built and solution annealed condition. Thus, in the following the microstructure of the brazing alloy is analyzed based in the as-built state. The solution-annealed condition is mentioned only if there are any differences.

Fig. 8 compares the location of the brazing filler metal application of a laser-melted wetting sample to that of a conventional wetting sample. On the laser-melted wetting samples, the brazing filler metal solidifies as a polycrystalline, cellular nickel solid solution. Spherical chromium borides precipitate in the valleys between the grains. The chemical composition of the phases can be found in Table 5.

Due to the cellular solidification of the brazing alloy, the surface topography of the laser-melted sample appears dimpled. This is in contrast to the solidification morphology of the conventional wetting samples. There, the surface topography of the braze droplet is more uniform as a result of an equiaxial dendritic solidification. In addition, the braze droplet is characterized by the precipitation of chromium borides and nickel silicides. Nickel silicides were not present in the

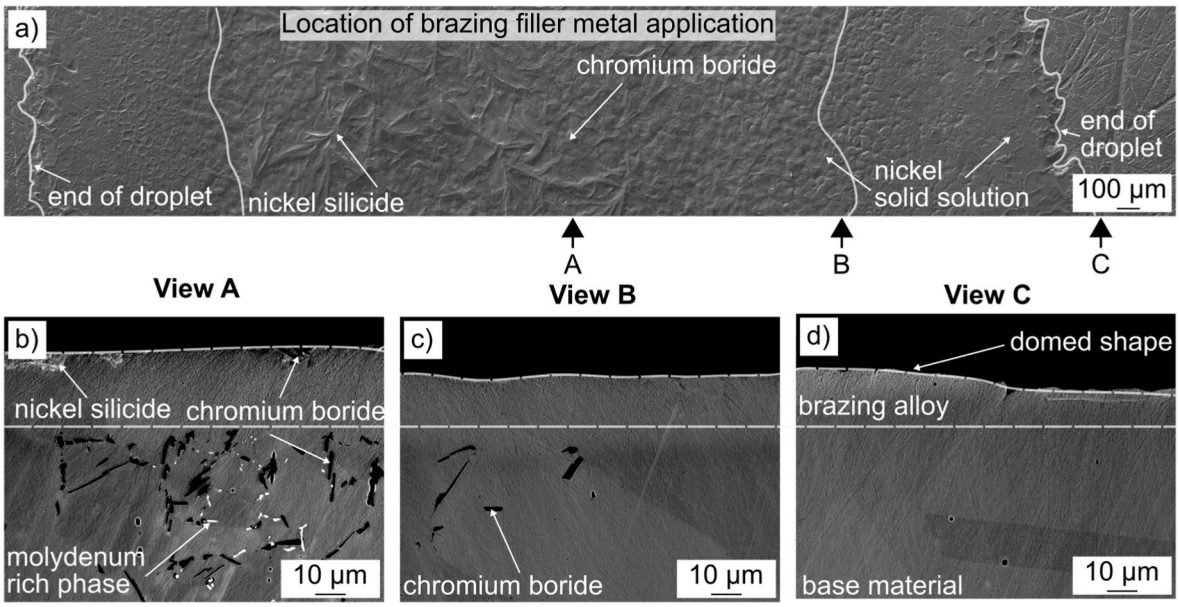

Fig. 5. Top view and cross-section of the brazing alloy on a conventional wetting sample.

Table 4
Chemical Composition of the Phases in wt-%.

Phase	Ni	Cr	Si	B	Fe	Mn	Mo
Nickel solid solution	46.6	13.9	2.4	0.0	26.8	0.2	0.3
Nickel silicides	59.3	7.8	6.2	0.0	17.2	0.0	0.0
Chromium borides	14.7	39.4	1.1	1.5	16.1	0.0	5.4
Mo-rich phase	6.0	20.3	0.0	1.6	46.6	1.4	11.4

solidified braze droplet of the laser-melted wetting samples. Moreover, the chromium borides showed a different morphology. The reason for the differences in the solidification morphology of the brazing alloy and the precipitated phases (chromium borides, nickel silicides) is the solidification rate of the brazing filler metal. Needle-shaped precipitates and an equiaxial-dendritic solidification structure indicate a higher solidification rate of the brazing filler metal on the conventional wetting samples [40–42].

Fig. 9 shows the location of the brazing filler metal application in the cross-section. Similar to the conventional wetting samples, the brazing alloy crystallizes directly on the surface of the laser-melted material. Starting from there, it grows continuously upwards. This continuous growth is a further indicator of cellular solidification [42]. In contrast, the equiaxial dendritic grain structure of the brazing alloy on the conventional wetting samples is characterized by multi-layered solidified grains (see Fig. 9b). As with the conventional material, chromium borides precipitate at the grain boundaries of the laser-melted base material. Contrary to the chromium borides above the nickel solid solution, the chromium borides in the base material have the same block-like shape as in the conventional wetting samples. The molybdenum-containing phase which was precipitated along the grain boundaries of the conventionally cast base material is not present in the laser-melted wetting samples.

The chemical composition of all detected phases determined by WDX can be found in Table 5. Compared to the conventional wetting samples, the nickel solid solution of the laser-melted wetting samples tends to have lower levels of the brazing filler constituent silicon and higher levels of the base metal constituents iron and chromium. One possible explanation for the differences in the element contents are stronger diffusion processes of the brazing filler metal with the laser-melted material. This could be due to the higher number of grain boundaries at the surface of the laser-melted material in the as-built condition [9]. Since diffusion during brazing occurs primarily along grain boundaries [20], a larger number of grains results in a larger diffusion cross-section. This enhances the diffusion between the brazing filler metal and the laser-melted material.

The assumption of stronger diffusion processes is confirmed by the chemical composition of the base materials in the area affected by the brazing filler metal. There, the laser-melted material has a higher

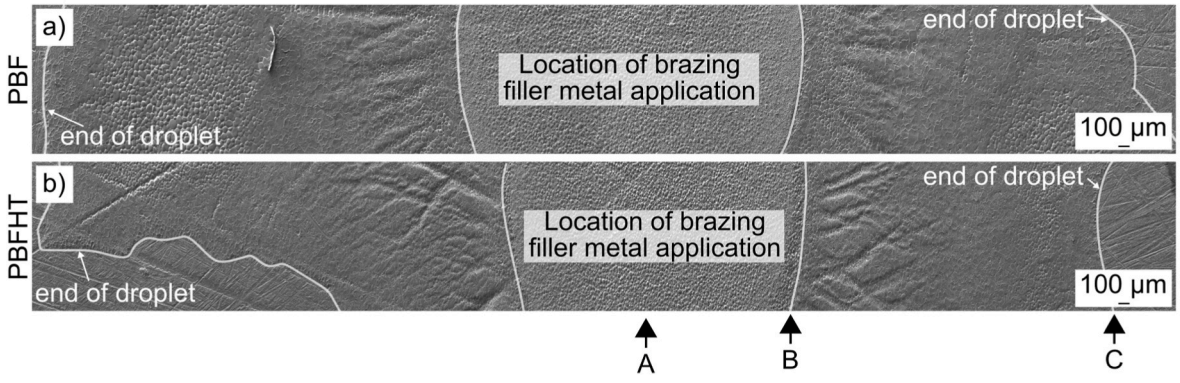

Fig. 6. Top View of the laser-melted Wetting Samples.

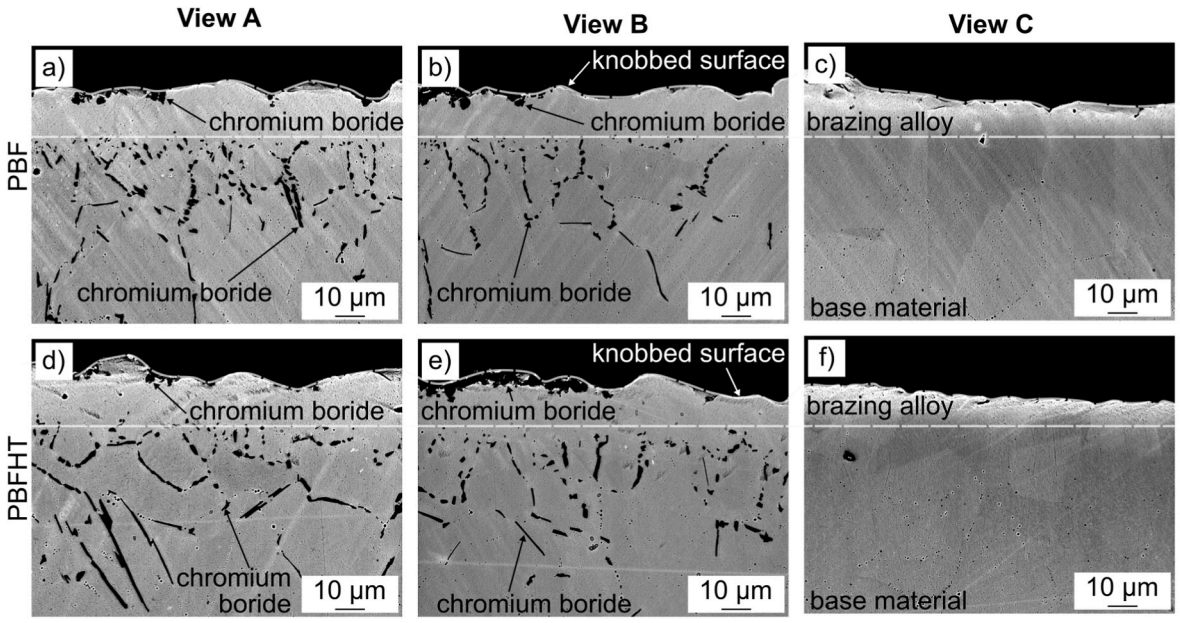

Fig. 7. Cross-section of the laser-melted Wetting Samples.

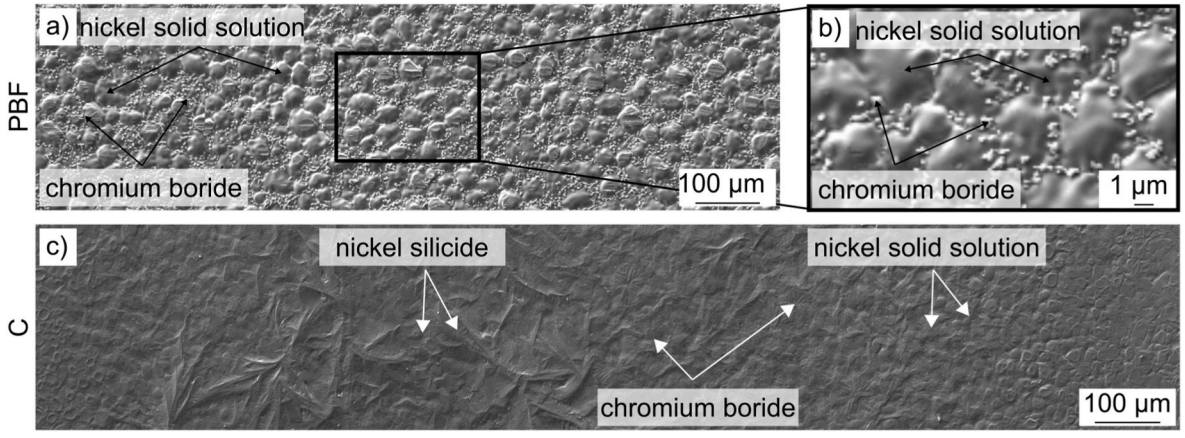

Fig. 8. Top View of the Center of the Braze Alloy of a (a), (b) laser-melted and (c) conventional Wetting Sample.

Table 5
Chemical Composition of the Phases on the laser-melted Wetting samples in wt-%.

Sample	Phase	Ni	Cr	Si	B	Fe	Mn	Mo
C	Nickel solid solution	46.6	13.9	2.4	0.0	26.8	0.2	0.2
PBF	Nickel solid solution	44.1	15.9	1.9	0.0	27.4	0.2	0.5
PBFHT	Nickel solid solution	41.4	17.4	1.7	0.0	29.9	0.2	0.6
C	Chromium borides	2.0	49.7	0.0	1.2	27.2	0.6	2.3
PBF	Chromium borides	2.8	48.9	0.0	1.1	28.0	0.6	1.5
PBFHT	Chromium borides	2.8	47.5	0.0	1.1	25.6	1.4	1.7
C	Base material in diffusion zone	10.0	15.4	0.1	0.0	61.0	2.0	1.3
PBF	Base material in diffusion zone	17.6	16.0	0.8	0.0	54.0	0.5	1.1
PBFHT	Base material in diffusion zone	13.1	17.6	0.6	0.0	58.7	0.6	1.3

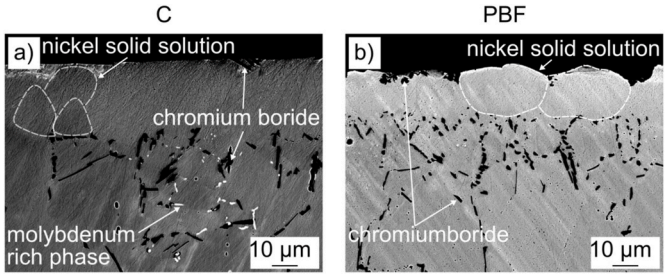

Fig. 9. Center of the Brazing Alloy Droplet in the Cross-section of a (a) laser-melted and (b) conventional Wetting Sample.

content of silicon and a lower content of iron compared to the conventionally cast material. The higher silicon content of the base material could also be the reason why no nickel silicides were observed in the laser-melted wetting samples.

There are slight variations in the chemical composition of the different phases between the laser-melted material states as-built and solution-annealed. However, based on the chemical compositions, there

is no recognizable trend as to whether one of the material states has a stronger mass transfer with the brazing filler metal.

Outside the area of brazing filler metal application, the solidification morphologies of the conventional and laser-melted wetting samples differ considerably. Therefore, a further direct comparison of the brazing filler metal's solidification structures is not possible. For this reason, the solidification structure of the brazing filler metal on the laser-melted wetting samples is primarily considered below.

In the laser-melted wetting samples, the end of the brazing filler metal application area is indicated by a light silver edge under the light microscope, see Fig. 10a. Using the scanning electron microscope, it can be seen that the chromium borides that have been precipitated on top of the nickel solid solution abruptly disappear (Fig. 10b). In addition, the morphology of the nickel solid solution changes from cellular to equiaxial dendritic. A reason for the sudden disappearance of the chromium borides could be the decreasing brazing metal volume from the center of the droplet towards the edge and the solubility of the boron in the molten brazing filler metal.

Beyond the location of brazing filler metal application, the appearance of the solidified braze droplet is characterized by vein-like structures. The light microscopic images in Fig. 11 show that the vein-like structures run in a circular pattern away from the brazing filler metal application site. The shape of these structures is linear or branched. The length of the linear structures appears optically longer than that of the vein-like branched structures. In the literature, only Ambrose et al. has observed a similar solidification structure in wetting tests of the nickel-based brazing filler metal Ni11P on the steel Fe2Cr [43,44]. They did not specify a cause for the formation of the solidification structure.

A marking of grinding grooves on the material surface in Fig. 11c shows a correlation to the linear structures. The linear structures preferably form in the direction of the greatest brazing metal flow along the direction of propagation of the grinding grooves. Consequently, the grinding grooves have a wetting-promoting influence. This influence is caused by a capillary effect induced in them [43]. In the case of the vein-like branched structures, no influence of the grinding grooves is recognizable. Regardless of the grinding direction, the vein-like branched structures run in a circular pattern away from the brazing filler metal application site. The correlations shown are also observable in the SEM images in Fig. 12.

At higher magnification in Fig. 13, it is visible that the vein-like structures are grooves. These grooves are more pronounced in the solution-annealed state than in the as-built condition (see Fig. 13a/b). Differences between the linear and the vein-like branched grooves become visible in closer inspection of the topographies: While the linear grooves run in a straight line, the vein-like grooves follow the curvature of the grain boundaries.

Neither the linear nor the branched grooves were observed on the conventional wetting samples. Their existence could explain the better spreading behavior of the brazing filler metal on the laser-melted 316L alloy. The correlation with the grinding grooves on the material surface provides an indication of the formation of the linear grooves.

The surface topography of the base materials after the wetting test provides a possible clue to the formation of the vein-like branched grooves. Fig. 14 compares the joint surfaces of all base materials at positions without brazing material.

Grain boundaries are visible on all joint surfaces after wetting tests without etching. The visibility of the grains without the use of metallographic etching indicates diffusion processes that took place on the joint surface due to the effect of temperature during the brazing cycle.

The grain boundaries are more pronounced in both additive material states (as-built, solution-annealed) than in the conventionally cast material. A difference between the laser-melted material states is not visually recognizable. The varying characteristics of the grain boundaries between the conventional and the laser-melted base materials indicate different levels of diffusion processes on the joint surface.

3.4. Surface diffusion mechanisms

Due to the surface preparation of all wetting samples by means of a grinding process, it can be assumed that the grain boundaries were smoothly flushed with the joining surface prior to testing (see principle schematic in Fig. 16a). The topographical differences between the joint surfaces of the conventional and laser-melted base materials must therefore result from the brazing process. In the case of the solution-annealed laser-melted material, the previous heat treatment must also be considered.

In order to analyze whether the topographical differences have formed during the wetting tests, polished samples without brazing material were subjected to the same brazing cycle as the wetting samples. Under SEM magnification, these topographical differences are recognizable as grooves at the grain boundaries in Fig. 15. At the same scale as the laser-melted materials, a grain boundary groove on the conventional base material is barely visible.

Grain boundary grooves of varying sizes may explain the enhanced wettability of laser-melted 316L. During the spreading process of the molten filler metal, a capillary effect could occur in the grain boundary grooves. This could promote wetting at the joint surface. Such a wetting promoting effect is known for grinding grooves [45–47].

A capillary effect could promote the flow of the brazing material across a large number of differently oriented grain boundary grooves. According to the principle of least resistance, this could result in a vein-like branched flow of the brazing material, which is reflected in the solidified structure as a correspondingly shaped groove.

Grain boundary grooving is a known diffusion mechanism in literature. Under the influence of temperature, a groove forms between two grains that intersect a surface in a polycrystalline material [48]. Grooving begins above a threshold temperature that corresponds to more than 50 % of the melting temperature of the material [49,50]. The stainless steel 316L has a melting range of 1390 °C–1440 °C (1663 K–1713 K) [51]. Therefore, groove formation begins above the temperature interval of 559 °C–584 °C (832 K–857 K). During the wetting tests, the brazing temperature of 1190 °C was above this threshold temperature.

The driving force for groove formation is the general desire of a

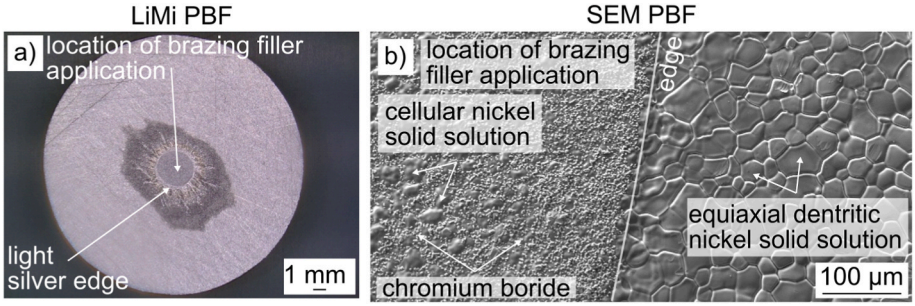

Fig. 10. End of the brazing filler metal application.

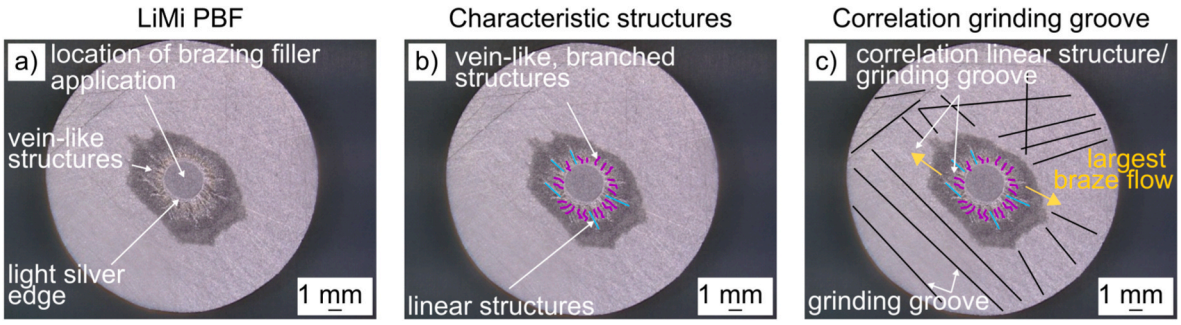

Fig. 11. Vein-like Structures of solidified braze droplets.

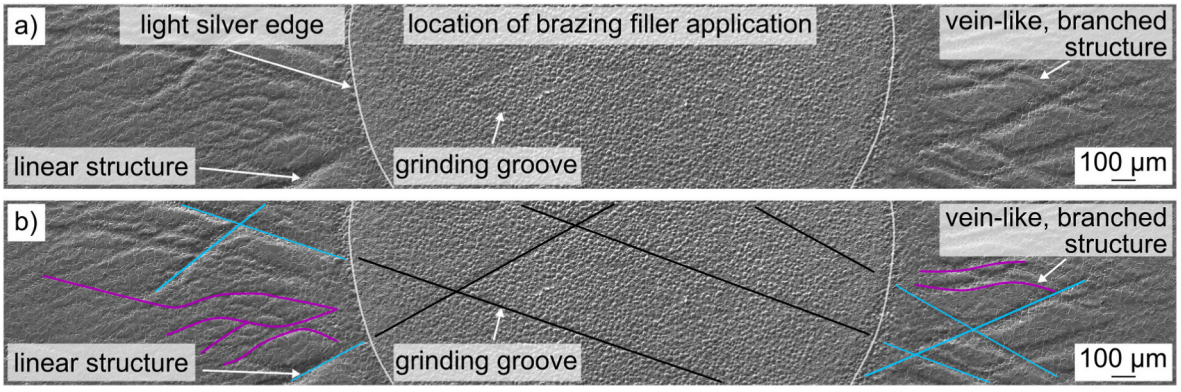

Fig. 12. SEM - Top view - Vein-like Structures.

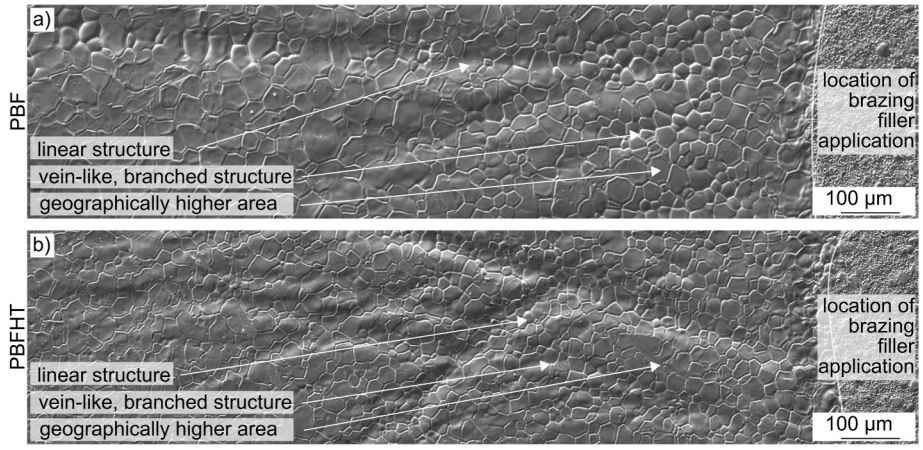

Fig. 13. Vein-like Structures: (a) as-built and (b) solution-annealed Sample.

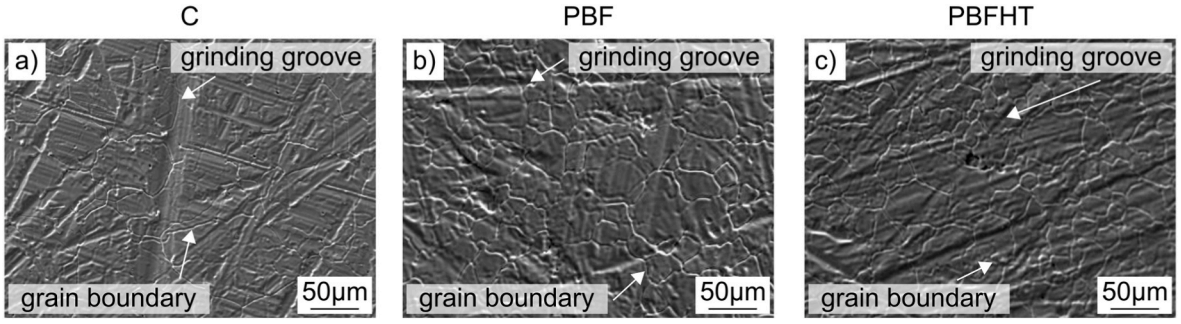

Fig. 14. Top view of base materials without brazing alloy - SEM

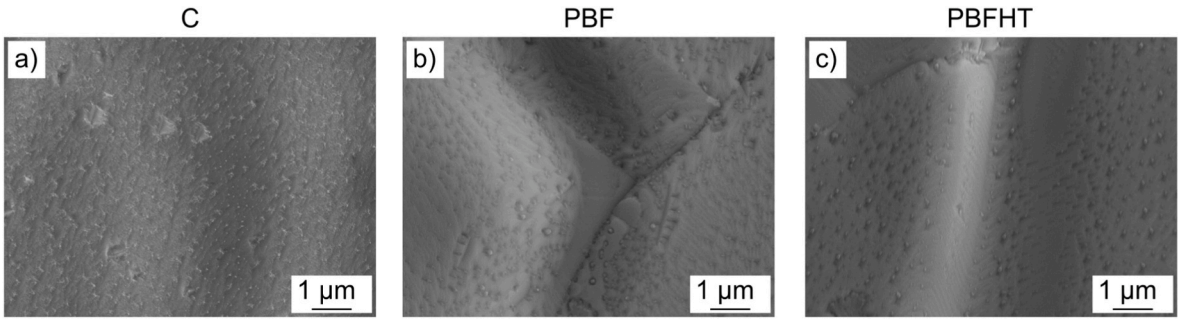

Fig. 15. Grain boundary grooves - top view - SEM

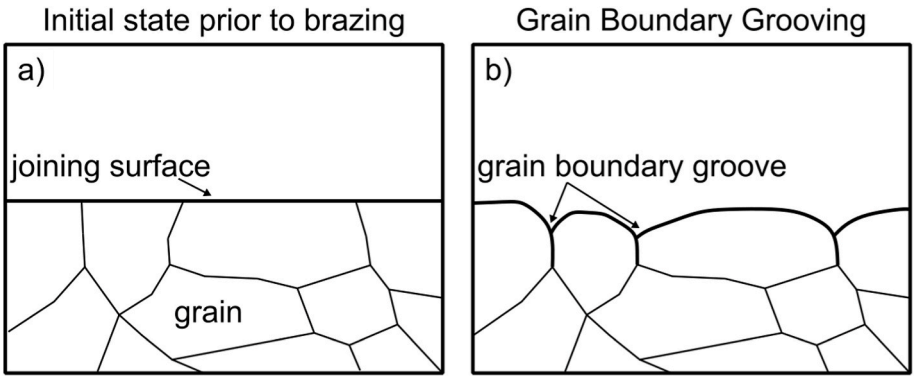

Fig. 16. Principle Sketch of Groove Formation based on Grain Boundary Grooving.

surface to reduce its free energy [50,52–54]. Groove growth is based on the vaporization or diffusion of atoms at a grain boundary [50,53]. Fig. 17 shows a principle sketch of the geometry of a grain boundary groove formed by the surface diffusion mechanism. This kind of grain boundary groove is defined by the parameters 'width b', 'depth h' and 'opening angle β'.

The shape of a grain boundary groove is constant regardless of the duration of heat exposure [48,53]. However, the groove parameters (width b, depth h and opening angle β) change with time [48,53], temperature and the surface energy of the material [48]. Since both the surface energy and the duration of heat exposure vary between the conventional and the laser-melted material states (as-built, solution-annealed), it can be assumed that the differently pronounced grooves on the surface of the base materials are attributable to grain boundary grooving. In order to verify the diffusion mechanism, the topography of the grain boundary grooves of all the base materials was measured by means of atomic force microscopy (AFM). Fig. 18 illustrates sample groove profiles of all base materials after a brazing cycle.

The topography of the grain boundary grooves are similar to the shape shown in Fig. 17. The groove parameters shown in Fig. 19 also correspond to the orders of magnitude described in various publications [36,48,50,55–58]. For this reason, it is assumed that the grooves were formed as a result of the diffusion mechanism grain boundary grooving.

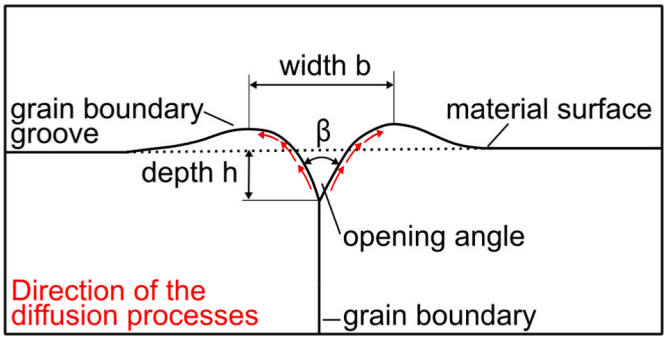

Fig. 17. Principle sketch - geometry of a grain boundary groove [48,52].

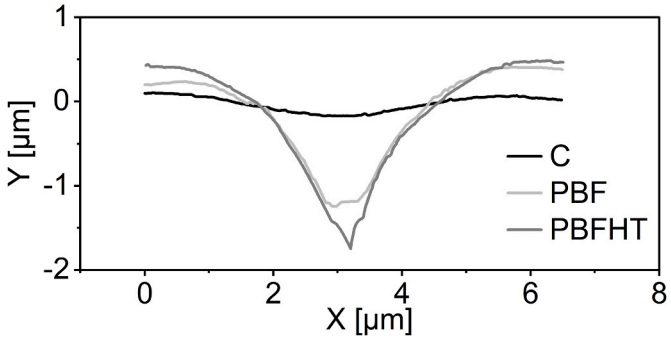

Fig. 18. Topography of the grain boundary grooves.

For both laser-melted material states, the average groove depth h is greater than for the conventionally cast material. The groove width is not significantly different.

On the solution-annealed laser-melted material, the grain boundary grooves are 67 % deeper and have an 18 % sharper opening angle than in the as-built condition. The reason for the increased development of the groove parameters is the higher overall heat exposure of the solution-annealed material [48,53]. The greater groove formation in both laser-melted material states leads to a larger effective grain boundary area on the joint surface. This is the reason why the additive material exhibits a greater diffusion of the brazing filler metal.

The brazing material flow along a grain boundary groove is largely determined by the groove characteristics. Spontaneous local acceleration in a grain boundary groove only occurs if the opening angle β of the groove is greater than the contact angle θ between the brazing filler

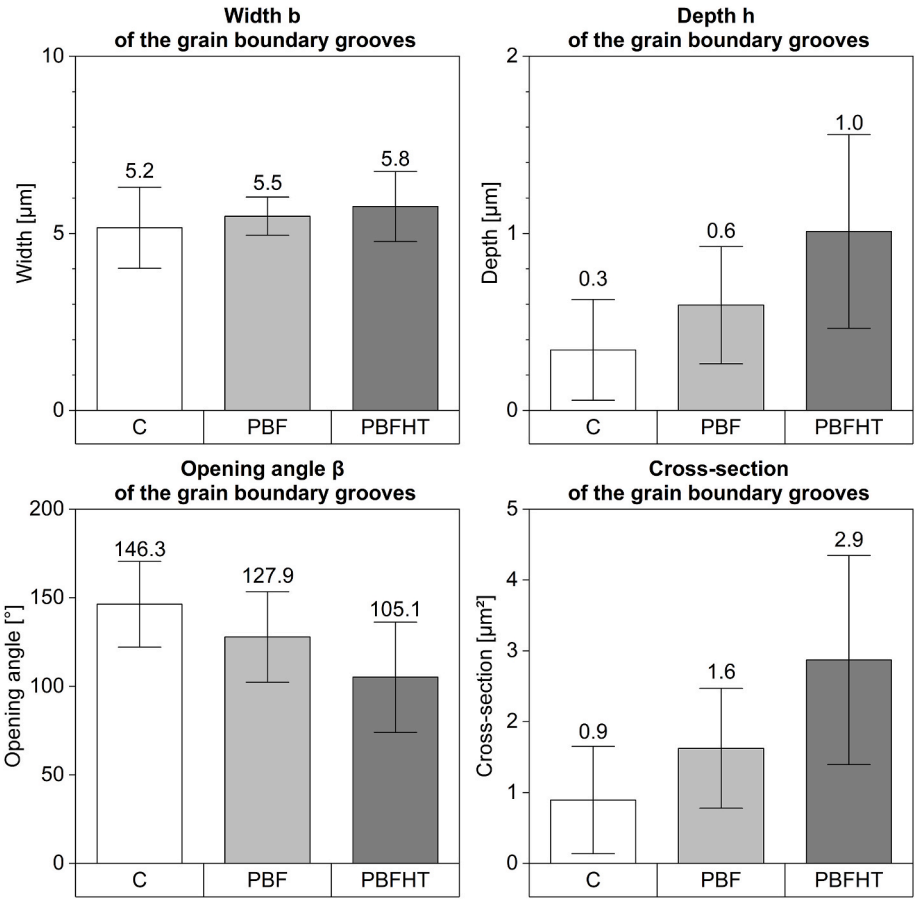

Fig. 19. Groove characteristics and cross-section of the grain boundary grooves.

metal and the base material [46,47]. In addition, the opening angle of the grain boundary groove is decisive for the extent of liquid braze alloy transport. The larger it is, the worse the local acceleration of the liquid brazing filler metal in the groove [45]. The evaluation of the opening angle β of the grain boundary grooves shows that for all base materials the opening angle is greater than the measured contact angle θ between the brazing filler metal and the respective base material ($\beta_{K,\ PBF,\ PBFBW} > 100° > \theta_K$: 2.5° or $\theta_{PBF,\ PBFWB}$: 1.2°). Thus, the conditions for a spontaneous local acceleration of the molten brazing material along the grain boundary grooves are fulfilled for all base materials [46,47].

The groove geometry determines the amount of the molten brazing metal volume that can be transported via the groove cross-section. The larger the groove cross-section, the more brazing metal volume can be transported along a grain boundary groove. Therefore, large groove cross-sections have a stronger wetting-promoting influence. The cross-section of a grain boundary groove is smaller for the conventionally cast material than for the laser-melted materials (as-built, solution annealed), see Fig. 19 (bottom right). Consequently, the wetting-promoting influence is greater for both laser-melted material states.

Due to the larger groove cross-section in the solution-annealed laser-melted material, the wetting-promoting influence of the grain boundary grooves is higher than in the as-built state. This explains why this material state has the same wettability as the as-built state despite having a lower surface energy.

The total volume of brazing metal that can be transported is not only influenced directly by the groove cross-section, but also indirectly by the groove geometry. The groove geometry determines the magnitude of the capillary effect induced in a groove. Thus, the local acceleration of the filler metal along the grain boundary groove is also influenced. The greater the acceleration of the brazing filler metal in a grain boundary groove, the more brazing filler metal volume can be transported at a given groove cross-section. Since the induced capillary effect is the strongest at the bottom of a groove [45,46], the opening angle β of a grain boundary groove is particularly decisive for the acceleration of the molten brazing filler metal. The induced capillary effect in a groove decreases with an increasing rounding of the opening angle β [45]. With the increasing rounding of the opening angle, it also becomes more difficult to maintain the conditions for spontaneous local acceleration of the brazing filler metal over a longer period of time [46]. The opening angle of the grain boundary grooves is sharper in the laser-melted material than in the conventionally cast material. As a result, the induced capillary effect is greater and easier to maintain. In addition to the larger groove cross-section, this increases the wetting-promoting influence of a grain boundary groove. The same applies to the solution-annealed additive material. The grain boundary grooves are sharper in the solution-annealed material state than in the as-built condition.

4. Conclusion

The study demonstrates that the laser-melted 316L exhibits enhanced wettability with the nickel-based brazing filler metal B–Ni5a compared to the conventionally cast material. This results in a larger spreading area and a smaller contact angle of the brazing filler metal on the additive joining surface. The enhanced wettability is attributed to the higher surface energy of the laser-melted material in the as-built condition and a diffusion mechanism known as grain boundary grooving that occurs at elevated temperatures. When brazing, this diffusion mechanism results in grooves along the grain boundaries of a material's surface. These grain boundary grooves are more pronounced in the laser-melted material than in the conventionally cast material. They induce a capillary effect that further promotes the spreading of the brazing filler metal on the laser-melted surface.

The enhanced wettability of the laser-melted material is independent of whether it is in the as-built or solution-annealed condition. The investigations revealed equivalent wettability in both material states. The reason for this is the reciprocal influence of the surface energy of the joining surface and the grain boundary grooving. The surface energy of the solution-annealed laser-melted material is lower than in the as-built state. This is due to recovery processes of the material microstructure during heat treatment. According to Young's equation, a lower surface energy has a negative effect on the wettability of a material surface. On the other hand, the grain boundary grooves on the material surface of the solution-annealed material condition have a higher wetting-promoting influence, which is caused by more pronounced grooves characteristics compared to the as-built state.

For brazing technology, the improved wettability enables the production of high-strength brazed joints from laser-melted 316L alloy. As a result of the equivalent wettability of the two laser-melted material states (as-built and solution annealed), brazing can be performed in a single process step when using the nickel-based brazing filler metal B–Ni5a. Using this brazing filler metal, brazing is performed together with the solution annealing process of the laser-melted material, thereby saving time and costs.

Declaration of competing interest

The authors declare that they have no known competing financial interests or personal relationships that could have appeared to influence the work reported in this paper.

Acknowledgements

The contents presented were conducted within project TI 343-162-1 'Brazeability of similar hybrid joint compounds consisting of additively manufactured and conventional material grades' which is founded by the German Research Foundation (DFG). The sponsorship and support are gratefully acknowledged.

The authors further thank the DFG and the Ministry of Culture and Science of North Rhine-Westphalia (Ministerium fuer Kultur und Wissenschaft des Landes Nordrhein-Westfalen, NRW) for their financial support within the Major Research Instrumentation Program for the FIB-SEM (project no. 386509496) and the In-Situ-AFM (project no. 445052562).

References

[1] DIN EN ISO/ASTM 52900:2018-06. Additive manufacturing - general principles - terminology (ISO/ASTM DIS 52900:2018); German and English version prEN ISO/ASTM 52900:2018. Berlin: Beuth Verlag GmbH; 2018.
[2] DebRoy T, Wei HL, Zuback JS, Mukherjee T, Elmer JW, Milewski JO, Beese AM, Wilson-Heid A, De A, Zhang W. Additive manufacturing of metallic components – process, structure and properties. Prog Mater Sci 2018;92:112–224. https://doi.org/10.1016/j.pmatsci.2017.10.001.
[3] Celik E. Additive manufacturing: Science and technology. Berlin, Boston: Walter de Gruyter GmbH; 2020.
[4] Hopkinson N, Dickens P, editors. Analysis of rapid manufacturing—using layer manufacturing processes for production; 2003.
[5] Roberts T. Additive Manufacturing Trend Report 2021: 3D Printing Market Growth in the Year of the COVID-19. 2021.
[6] Thijs L. Microstructure and texture of metal parts produced by Selective Laser Melting. Löwen: Dissertation; 2014.
[7] Kruth J-P, Mercelis P, van Vaerenbergh J, Froyen L, Rombouts M. Binding mechanisms in selective laser sintering and selective laser melting. Rapid Prototyp J 2005;11:26–36. https://doi.org/10.1108/13552540510573365.
[8] Tillmann W, Henning T, Wojarski L, Bültena J. Vacuum brazing of 18MAR300 nickel maraging steel joints based on additively manufactured and conventional material grades. steel research int 2023;94:297. https://doi.org/10.1002/srin.202300108.
[9] Tillmann W, Bültena J, Wojarski L, Crasmöller A. Microstructure of conventional/PBF-LB/M 316L stainless steel hybrid joints brazed with nickel-based brazing alloys. Weld World 2023;1:3D. https://doi.org/10.1007/s40194-023-01652-x.
[10] American Welding Society. Brazing handbook. fourth ed. Miami, FL: American Welding Society; 1991.
[11] Shin W-S, Son B, Song W, Sohn H, Jang H, Kim Y-J, Park C. Heat treatment effect on the microstructure, mechanical properties, and wear behaviors of stainless steel 316L prepared via selective laser melting. Mater Sci Eng, A 2021;806:140805. https://doi.org/10.1016/j.msea.2021.140805.
[12] Ronneberg T, Davies CM, Hooper PA. Revealing relationships between porosity, microstructure and mechanical properties of laser powder bed fusion 316L stainless steel through heat treatment. Mater Des 2020;189:108481. https://doi.org/10.1016/j.matdes.2020.108481.
[13] Diepold B, Neumeier S, Meermeier A, Höppel HW, Sebald T, Göken M. Temperature-dependent dynamic strain aging in selective laser melted 316L. Adv Eng Mater 2021;23:2001501. https://doi.org/10.1002/adem.202001501.
[14] Penyaz MA, Ivannikov AA, Sevryukov ON, Kalin BA. Overview of nickel-based filler metals for brazing of austenitic stainless steels, nfm 2021:41–56. https://doi.org/10.17580/nfm.2021.01.06.
[15] Y. Li, Y. Shen, S. Zhong, X. Li, Y. Pei, L. Wang, Investigation on properties of joints vacuum brazed with nickel-based adhesive tape filler metal, in: 2021 3rd International conference on artificial intelligence and advanced manufacture, Manchester United Kingdom, ACM, New York, NY, USA, 10232021, pp. 2594–2598.
[16] Innobraze GmbH. Nickel based brazing pastes. https://innobraze.de/produkte/lotpasten/nickel/. [Accessed 23 November 2022].
[17] Saeidi K, Gao X, Lofaj F, Kvetková L, Shen ZJ. Transformation of austenite to duplex austenite-ferrite assembly in annealed stainless steel 316L consolidated by laser melting. J Alloys Compd 2015;633:463–9. https://doi.org/10.1016/j.jallcom.2015.01.249.
[18] Sun Z, Tan X, Tor SB, Yeong WY. Selective laser melting of stainless steel 316L with low porosity and high build rates. Mater Des 2016;104:197–204. https://doi.org/10.1016/j.matdes.2016.05.035.
[19] Jacobson DM, Humpston G. Principles of brazing. Materials Park, NY: ASM International; 2010.
[20] Sekulić DP, editor. Advances in brazing: Science, technology and applications. Cambridge, UK, Philadelphia, PA: Woodhead Publishing; 2013.
[21] Hebda M, Kaczor P, Miernik K. Archives of metallurgy and materials, institute of metallurgy and materials science of. Polish Academy of Sciences; 2019.
[22] Hartmann T, Nuetzel D. Nickel-chromium-based amorphous brazing foils for continuous furnace brazing of stainless steel. In: 9th international conference of brazing, high temperature brazing and diffusion bonding. Aachen; 2010. p. 42–7.
[23] Rabinkin A. High-temperature brazing: filler metals and processing. In: Sekulić DP, editor. Advances in brazing: Science, technology and applications. Cambridge, UK, Philadelphia, PA: Woodhead Publishing; 2013. p. 121–59.
[24] Weinstein M, Lee L, Skinner CJ, Osmanda AM, Battenbough AJ, Staines AM. Further developments in boron-free nickel-chromium-phosphorus-silicon brazing filler metals. 2012.
[25] Miyazawa Y, Ohta K, Nishiyama A. Effect of stainless steel chemical composition on brazing ability of filler metal. IOP Conf Ser Mater Sci Eng 2014;61. https://doi.org/10.1088/1757-899X/61/1/012014.
[26] Rabinkin A. Brazing with (NiCoCr)–B–Si amorphous brazing filler metals: alloys, processing, joint structure, properties, applications. Sci Technol Weld Join 2004;9:181–99. https://doi.org/10.1179/136217104225012300.
[27] Liu J, Liu G, Ouyang H, Li Y, Yan M, Pecht M. Wetting kinetics and microstructure analysis of BNi2 filler metal over selective laser melted Ti-6Al-4V substrate. Materials 2020;13. https://doi.org/10.3390/ma13204666.
[28] Hao L, Liu J, Li Y. Wetting and spreading of AgCuTi on selective laser-melted Ti-6Al-4V. Materials 2021;14. https://doi.org/10.3390/ma14174804.
[29] VACUUMSCHMELZE GmbH & Co. KG. Vitrobraze VZ2152. 2019. Hanau.
[30] Cui L, Jiang S, Xu J, Peng RL, Mousavian RT, Moverare J. Revealing relationships between microstructure and hardening nature of additively manufactured 316L stainless steel. Mater Des 2021;198:109385. https://doi.org/10.1016/j.matdes.2020.109385.
[31] Young T. An essay on the cohesion of fluids. Phil. Trans. R. Soc. 1805;95:65–87. https://doi.org/10.1098/rstl.1805.0005. III.
[32] (ISO 19403-2:2017); German version EN ISO 19403-2:2020 DIN EN ISO 19403-2: 2020-04, Paints and varnishes - wettability - Part 2: determination of the surface free energy of solid surfaces by measuring the contact angle. Berlin: Beuth Verlag GmbH; 2020.
[33] DIN EN ISO 19403-1:2022-09. Paints and varnishes - wettability - Part 1: vocabulary and general principles. Berlin: Beuth Verlag GmbH; 2022 (ISO 19403-1: 2022); German version EN ISO 19403-1:2022.
[34] Strodick S, Schmidt R, Donnerbauer K, Rozo Vasquez J, Zabel A, Macias Barrientos M, Biermann D, Walther F. Subsurface conditioning in BTA deep hole drilling for improved component performance. Prod Eng Res Dev 2024;18:299–317. https://doi.org/10.1007/s11740-023-01252-0.
[35] Lingnau LA, Heermant J, Otto JL, Donnerbauer K, Sauer LM, Lücker L, Macias Barrientos M, Walther F. Separation of damage mechanisms in full forward rod extruded case-hardening steel 16MnCrS5 using 3D image segmentation. Materials 2024;17. https://doi.org/10.3390/ma17123023.
[36] Handwerker CA, Dynys JM, Cannon RM, Coble RL. Metal reference line technique for obtaining dihedral angles from surface thermal grooves. J Am Ceram Soc 1990;73:1365–70. https://doi.org/10.1111/j.1151-2916.1990.tb05206.x.
[37] Neßlinger V, Welzel S, Rieker F, Meinderink D, Nieken U, Grundmeier G. Thin organic-inorganic anti-fouling hybrid-films for microreactor components. Macromol React Eng 2023;17:155. https://doi.org/10.1002/mren.202200043.
[38] Geenen K. Werkstofftechnische Charakterisierung austenitischer und martensitischer Stähle nach dem selektiven Laserschmelzen. Bochum: Dissertation; 2018.

[39] Gale WF, Wallach ER. Wetting of nickel alloys by nickel based brazes. Mater Sci Technol 1990;6:170–5. https://doi.org/10.1179/mst.1990.6.2.170.
[40] Seibert J. Nukleationsmechanismen der T1-Phase in der Aluminiumlegierung AA2195. Disseration. 2021.
[41] Kou S. Welding metallurgy. secondnd ed. Hoboken N.J.: Wiley-Interscience; 2003.
[42] Kurz W, Kurz W, Fisher DJ. Fundamentals of solidification, fourth., rev. ed., reprinted. Uetikon-Zuerich: Trans Tech Publ; 2005.
[43] Ambrose JC, Nicholas MG, Young N, Jenkins SL. Wetting and spreading of Ni–P brazes: effects of workpiece and braze composition. Mater Sci Technol 1990;6:1021–31. https://doi.org/10.1179/026708390790189533.
[44] Ambrose JC, Nicholas MG, Stoneham AM. Dynamics of liquid drop spreading in metal-metal systems. Acta Metall Mater 1993;41:2395–401. https://doi.org/10.1016/0956-7151(93)90319-N.
[45] Parker ER, Smoluchowski R. Capillarity of metallic surfaces. Transactions of the American Society for Metals 1945;35:362–73.
[46] Kitron-Belinkov M, Marmur A, Trabold T, Dadheech GV. Groovy drops: effect of groove curvature on spontaneous capillary flow. Langmuir 2007;23:8406–10. https://doi.org/10.1021/la700473m.
[47] Romero La, Yost FG. Flow in an open channel capillary. J Fluid Mech 1996;322:109–29.
[48] Mullins WW. Theory of thermal grooving. J Appl Phys 1957;28:333–9. https://doi.org/10.1063/1.1722742.
[49] Allen BC. Kinetics of grain boundary grooving in chromium, molybdenum, and tungsten. 1969.
[50] Tsoga A, Nikolopoulos P. Groove angles and surface mass transport in polycrystalline alumina. J Am Ceram Soc 1994;77:954–60. https://doi.org/10.1111/j.1151-2916.1994.tb07252.x.
[51] Sandmeyer Steel Company. Specification Sheet: Alloy 316/316L. 2014.
[52] Amram D, Klinger L, Gazit N, Gluska H, Rabkin E. Grain boundary grooving in thin films revisited: the role of interface diffusion. Acta Mater 2014;69:386–96. https://doi.org/10.1016/j.actamat.2014.02.008.
[53] Mullins WW. The effect of thermal grooving on grain boundary motion. Acta Metall 1958;6:414–27.
[54] Schölhammer J, Baretzky B, Gust W, Mittemeijer E, Straumal B. Grain boundary grooving as an indicator of grain boundary phase transformations. Interface Sci 2001;9:43–53.
[55] Rost MJ, Quist DA, Frenken JWM. Grains, growth, and grooving. Phys Rev Lett 2003;91:26101. https://doi.org/10.1103/PhysRevLett.91.026101.
[56] Mullins WW, Shewmon PG. The kinetics of grain boundary grooving in copper. Acta Metall 1959;7:163–70. https://doi.org/10.1016/0001-6160(59)90069-0.
[57] Klinger L, Rabkin E. Effects of surface anisotropy on grain boundary grooving. Interface Sci 2001;9:55–63.
[58] Haremski P, Epple L, Wieler M, Lupetin P, Thelen R, Hoffmann MJ. A thermal grooving study of relative grain boundary energies of nickel in polycrystalline Ni and in a Ni/YSZ anode measured by atomic force microscopy. Acta Mater 2021;214:116936. https://doi.org/10.1016/j.actamat.2021.116936.